

RESEARCH ARTICLE

10.1002/2016JB013124

Key Points:

- We map coseismic slip and early afterslip of the Illapel earthquake with InSAR and GPS
- Afterslip overlaps with coseismic slip and regions of high interseismic coupling, suggesting that frictional heterogeneities exist
- Deep coseismic slip and afterslip cause coastal uplift that may contribute in part to permanent coastal uplift

Supporting Information:

- Supporting Information S1
- Data Set S1
- Data Set S2
- Data Set S3
- Data Set S4
- Data Set S5
- Data Set S6

Correspondence to:

W. D. Barnhart,
william-barnhart-1@uiowa.edu

Citation:

Barnhart, W. D., J. R. Murray, R. W. Briggs, F. Gomez, C. P. J. Miles, J. Svarc, S. Riquelme, and B. J. Stressler (2016), Coseismic slip and early afterslip of the 2015 Illapel, Chile, earthquake: Implications for frictional heterogeneity and coastal uplift, *J. Geophys. Res. Solid Earth*, 121, 6172–6191, doi:10.1002/2016JB013124.

Received 26 APR 2016

Accepted 25 JUL 2016

Accepted article online 27 JUL 2016

Published online 16 AUG 2016

Coseismic slip and early afterslip of the 2015 Illapel, Chile, earthquake: Implications for frictional heterogeneity and coastal uplift

William D. Barnhart¹, Jessica R. Murray², Richard W. Briggs³, Francisco Gomez⁴, Charles P. J. Miles⁴, Jerry Svarc², Sebastian Riquelme⁵, and Bryan J. Stressler¹
¹Department of Earth and Environmental Sciences, University of Iowa, Iowa City, Iowa, USA, ²Earthquake Science Center, U.S. Geological Survey, Menlo Park, California, USA, ³Geological Hazards Science Center, U.S. Geological Survey, Golden, Colorado, USA, ⁴Department of Geological Sciences, University of Missouri, Columbia, Missouri, USA, ⁵Centro Sismológico Nacional, Universidad de Chile, Santiago, Chile

Abstract Great subduction earthquakes are thought to rupture portions of the megathrust, where interseismic coupling is high and velocity-weakening frictional behavior is dominant, releasing elastic deformation accrued over a seismic cycle. Conversely, postseismic afterslip is assumed to occur primarily in regions of velocity-strengthening frictional characteristics that may correlate with lower interseismic coupling. However, it remains unclear if fixed frictional properties of the subduction interface, coseismic or aftershock-induced stress redistribution, or other factors control the spatial distribution of afterslip. Here we use interferometric synthetic aperture radar and Global Position System observations to map the distribution of coseismic slip of the 2015 M_w 8.3 Illapel, Chile, earthquake and afterslip within the first 38 days following the earthquake. We find that afterslip overlaps the coseismic slip area and propagates along-strike into regions of both high and moderate interseismic coupling. The significance of these observations, however, is tempered by the limited resolution of geodetic inversions for both slip and coupling. Additional afterslip imaged deeper on the fault surface bounds a discrete region of deep coseismic slip, and both contribute to net uplift of the Chilean Coastal Cordillera. A simple partitioning of the subduction interface into regions of fixed frictional properties cannot reconcile our geodetic observations. Instead, stress heterogeneities, either preexisting or induced by the earthquake, likely provide the primary control on the afterslip distribution for this subduction zone earthquake. We also explore the occurrence of coseismic and postseismic coastal uplift in this sequence and its implications for recent hypotheses concerning the source of permanent coastal uplift along subduction zones.

1. Introduction

Numerous studies of subduction zone earthquakes since the 1960s have led to, among others, two first-order questions: What physical mechanism(s) control the various styles of slip (i.e., coseismic slip, afterslip, steady creep, and episodic slip) observed throughout the subduction zone earthquake cycle, and to what degree, if at all, do subduction zone earthquakes contribute to permanent deformation of the overriding plate?

Two broadly defined views have emerged to explain the timing and location of different slip styles on the subduction megathrust by invoking frictional properties. One view is the asperity model which stipulates that the megathrust is partitioned into regions that support rapid seismogenic slip (asperities) and surrounding regions that slip slowly and aseismically as either afterslip or interseismic creep [e.g., Lay and Kanamori, 1981; Savage, 1983; Scholz, 1998]. Rate and state friction provides a mechanical framework for understanding this model [e.g., Tse and Rice, 1986; Rice, 1993; Scholz, 1998]: the full rate and state formulation describes the dependence of fault frictional resistance on sliding velocity and state, the latter of which is interpreted as the age and quality of asperity contacts on the slip surface. Postseismic deformation models often use a simpler formulation in which the steady state dependence of fault frictional resistance on the logarithm of slip velocity is usually denoted as the difference of two rate and state constitutive parameters ($a - b$) [e.g., Scholz, 1998]. When ($a - b$) is negative, an increase in slip velocity results in lower friction, a condition termed velocity weakening. Conversely, when ($a - b$) > 0 the fault exhibits velocity-strengthening behavior, where a velocity increase causes friction to evolve to a higher value. Unstable, coseismic slip can nucleate only within velocity-weakening areas, although it may propagate into velocity-strengthening regions of the fault under certain conditions.

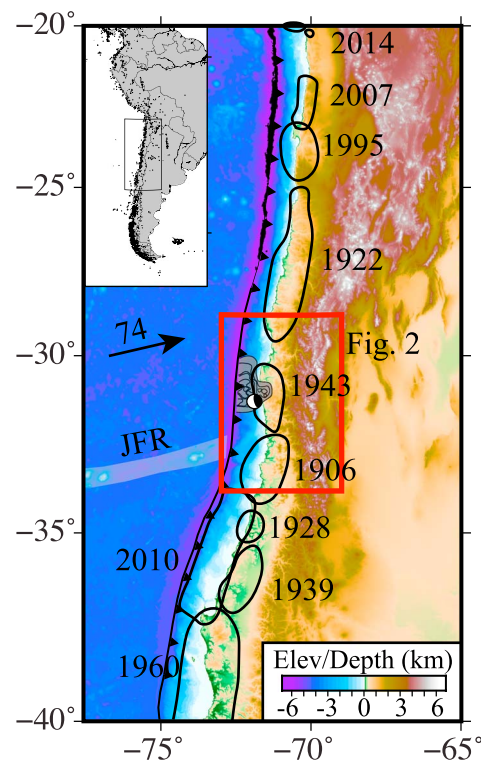


Figure 1. Seismotectonic context of the 2015 Illapel earthquake, which is denoted by the moment tensor solution [Ekström *et al.*, 2012]. The black outlines show the approximate extent of large subduction zone earthquakes in the 20th and 21st centuries [Kelleher, 1972; Motagh *et al.*, 2010; Tong *et al.*, 2010; Hayes *et al.*, 2014]. The Juan Fernandez Ridge (JFR) is outlined in gray. Image overlain on GEBCO topography and bathymetry. The moment tensor solution is for the Illapel earthquake [Ekström *et al.*, 2012]. The map inset shows the location of the study region, the velocity of the Nazca Plate relative to stable South America in mm/yr [DeMets *et al.*, 2010], and regional seismicity from the ISC GEM catalog [Storchak *et al.*, 2013]. The gray-shaded region shows the rupture area and smoothed 1 m contours of coseismic slip of the 2015 Illapel earthquake inferred from this study. The red box shows the spatial extent of Figure 2.

Velocity-strengthening areas slip stably, for example, via afterslip or interseismic creep, and act to arrest coseismic rupture. In a rate and state context, seismogenic asperities are often assumed to represent spatially fixed, unstable, velocity-weakening regions, while afterslip and continuous interseismic creep occupy stably slipping, velocity-strengthening zones [e.g., Boatwright and Cocco, 1996; Igarashi *et al.*, 2003; Chlieh *et al.*, 2007].

These expectations are further extended to relate interseismic coupling to the frictional characteristics of a fault, with the expectation that strong coupling indicates zones of velocity weakening behavior, while poorly coupled regions are velocity strengthening [e.g., Scholz, 1998; Perfettini and Avouac, 2007; Kaneko *et al.*, 2010]. Together, these models, using the simple implementation of steady state rate dependence, predict that coseismic slip and afterslip should not overlap across large regions of a fault, coseismic slip should occur in regions of high interseismic coupling, and afterslip should dominate regions of low coupling. Moreover, the frictional description of the asperity model broadly predicts that afterslip should occur both downdip and updip (i.e., near the trench) of the seismogenic zone, where the megathrust would occupy a velocity-strengthening frictional regime, as inferred from pressure and temperature considerations [e.g., Marone *et al.*, 1991; Scholz, 1998; Chlieh *et al.*, 2004; Hsu *et al.*, 2006].

Observations from many earthquakes support these models, particularly where interseismic coupling varies substantially in a way that correlates to coseismic slip distributions and where inferred afterslip overlaps little with imaged coseismic slip [Yagi *et al.*, 2003; Chlieh *et al.*, 2004; Miyazaki *et al.*, 2004; Bürgmann *et al.*, 2005; Baba *et al.*, 2006; Hsu *et al.*, 2006; Murray and Langbein, 2006; Moreno *et al.*, 2010; Loveless and Meade, 2011].

The second view of coseismic slip and aseismic afterslip, proposed by Helmstetter and Shaw [2009], stipulates that frictional characteristics of the megathrust are not steady state. This view is in part motivated by the observation that regions of afterslip and coseismic slip appear to overlap significantly in some earthquake sequences, implying that a simple, fixed frictional description of asperities cannot fully reconcile the spatial distribution of coseismic and postseismic slip [e.g., Bürgmann *et al.*, 2002; Hsu *et al.*, 2006; Pritchard and Simons, 2006; Johnson *et al.*, 2012, 2016; Bedford *et al.*, 2013; Lin *et al.*, 2013]. Through numerical simulations that implement a full rate and state formulation, Helmstetter and Shaw [2009] show that several factors, including stress heterogeneities imposed by the coseismic rupture itself or by previous earthquakes, likely control the spatial distribution of aseismic afterslip. They find that modeled coseismic and postseismic deformation associated with earthquakes can be fit using a wide range of values for rate and state parameters, even without appealing to spatial or temporal variations or strict adherence to rate-strengthening or rate-weakening steady state conditions.

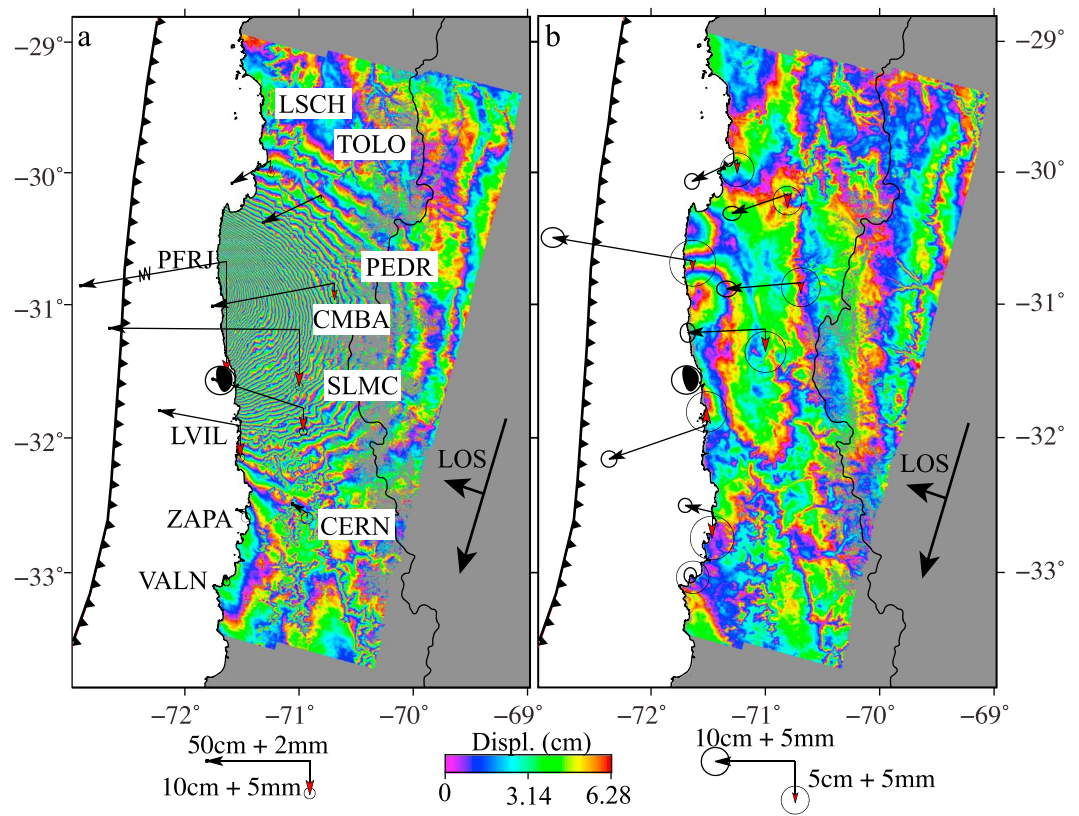


Figure 2. Descending (a) coseismic and (b) postseismic Sentinel-1a interferograms and three-dimensional static GPS displacements of the Illapel earthquake sequence. The interferograms span the time period of 24 August 2015 to 17 September 2015 (Figure 2a) and 17 September 2015 to 11 October 2015 (Figure 2b). GPS station names are denoted. The coseismic horizontal displacement of PFRJ is truncated for figure clarity. The moment tensor is the global CMT solution [Ekström *et al.*, 2012]. All GPS displacements shown are available in Table 1. The double arrows show the satellite along-track azimuth and line-of-sight (LOS) look direction.

In this study, we address the mechanical controls that affect coseismic slip and afterslip in the context of the 2015 Illapel, Chile, earthquake (Figure 1). The Illapel earthquake (M_w 8.3, 16 September 2015, 22:54:32 UTC; U.S. Geological Survey (USGS) National Earthquake Information Center) occurred in the central South American subduction zone, north of the 2010 M_w 8.8 Maule earthquake, an M_s 7.8 earthquake in 1939, and the region where the Juan Fernandez Ridge begins to subduct (Figure 1) [Beck *et al.*, 1998; Heidarzadeh *et al.*, 2016; Melgar *et al.*, 2016; Tilmann *et al.*, 2016]. The earthquake ruptured a portion of the subduction zone in the vicinity of that inferred to have last ruptured in 1943 (M_s 7.8–7.9) and where interseismic coupling is high [Beck *et al.*, 1998; Métois *et al.*, 2012; Tilmann *et al.*, 2016]. We use geodetic observations from Global Positioning System (GPS) and interferometric synthetic aperture radar (InSAR) to map the spatial distribution of coseismic slip and early afterslip (origin time (OT) + 1–38 days; Figure 2). We then explore the applicability of various proposed mechanical controls on the occurrence of coseismic or aseismic fault slip, and we address the impacts of fault slip inversion resolution on these interpretations.

We also examine the potential significance of recorded coseismic and postseismic coastal uplift during the Illapel sequence. Increasingly, researchers have found that slip in subduction zone earthquake sequences may contribute to permanent deformation of the fore arc [Loveless *et al.*, 2009; Baker *et al.*, 2013; Aron *et al.*, 2015]. However, it is unclear how these ruptures contribute to permanent coastal uplift, if at all. Subduction zone earthquakes commonly generate coastal subsidence [e.g., Plafker and Savage, 1970], and the subduction zone earthquake cycle is generally presumed to involve elastic deformation [e.g., Savage, 1983]. Yet coastlines above subduction zones experience net permanent uplift over millennial time scales [e.g., Kelsey *et al.*, 1994; Melnick, 2016]. We discuss the Illapel sequence in the context of a recent hypothesis

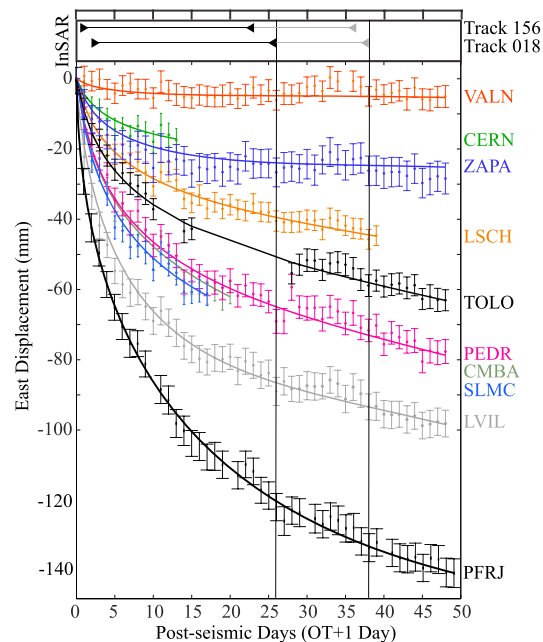


Figure 3. Postseismic InSAR observation intervals and GPS time series (east component only), point position uncertainties, and time series fits for the stations shown in Figure 2. The vertical bars indicate the time intervals at which we generate static postseismic GPS displacements (Figure 2b). The onset of modeled postseismic deformation is fixed to the origin time of the earthquake (15 September 2015 22:54:32 GMT; USGS NEIC). Full time series and time series fits are shown in Figure S1. Note that the time series of station CMBA resumes 61 days after origin time (Figure S1).

were estimated using Jet Propulsion Laboratory/NASA's GNSS-Inferred Positioning System-Orbit Analysis Simulation Software II software and final orbit and clock files; daily and 5 min kinematic point positions are available from the USGS and the corresponding author (http://earthquake.usgs.gov/monitoring/gps/Chile_2015).

We fit the three-component (ENU) time series of each station using the methodology of *Langbein et al.* [2006] in order to obtain static coseismic offsets, cumulative postseismic offsets, and associated uncertainties. For each time series we first estimated a constant velocity, coseismic offsets (Table S1), seasonal terms, and the amplitude of a logarithmic decay function with a fixed time constant (τ ; equation (1) of *Langbein et al.* [2006]) of 9×10^{-4} years (~ 8 h; Figures 3 and S1). The logarithmic decay is an empirically derived representation of the postseismic signal, and the time constant can be interpreted as the time delay between the coseismic step and the onset of the logarithmic decay. The time series analysis accounts for temporally correlated noise using a noise model that combines white, flicker, and random walk processes. This provides more realistic uncertainties on the estimated coseismic offsets and postseismic decay than if only white noise was considered. While it is possible to simultaneously estimate the noise amplitudes and the parameters being fit to the data [*Langbein*, 2004], doing this accurately requires substantially longer time series than our data set provides [*Langbein*, 2012]. Therefore, we assume amplitudes for the white and colored noise based on analyses of continuous GPS data from several other networks. We then used the estimated quantities to calculate the cumulative postseismic displacements and uncertainties at intervals of 1–26 and 1–38 days following the earthquake to coincide with available InSAR observations (Figures 2b and 3 and Table S1). We only invert cumulative postseismic static displacements from the eight stations that were operational for the first 38 days following the earthquake (Figure 3).

2.2. InSAR Observations

Coseismic and postseismic interferograms were generated from the Sentinel-1a C-band radar. We processed interferograms from descending track 156 and ascending track 018 (Figures 2 and S2a and Table S2) that were acquired in the Terrain Observations with Progressive Scans in azimuth (TOPS) mode. Fortunately,

that poses that coseismic ruptures and afterslip that propagate downdip of the seismogenic zone may contribute to permanent coastal uplift [e.g., *Sawai et al.*, 2004; *Kelsey et al.*, 2006; *Melnick*, 2016].

2. Observations and Modeling

To investigate the spatial characteristics of slip and surface deformation associated with the Illapel earthquake, we obtained GPS observations from a network of continuously recording instruments operated by the Centro Sismológico Nacional de la Universidad de Chile. These observations were supplemented with spatially dense InSAR observations derived from the European Space Agency's Sentinel-1a C-band radar.

2.1. GPS Observations

We generated position time series from 10 continuously operating GPS stations along the Chilean coast (Figures 2 and 3 and Figure S1 and Table S1 in the supporting information). Daily point positions and associated uncertainties

the first postearthquake acquisition occurred 11 h after the earthquake (17 September 2015, 10:03:45 UTC, track 156), allowing us to capture early postseismic displacements (Figure 2b). The largest aftershocks of the Illapel earthquake within our observation period (M_w 6.4–7.0) likewise occurred within this 11 h window; thus, the postseismic displacements are unlikely to be substantially influenced by aftershock-induced deformation. The tight temporal bounds of observations also allow us to model the slip distribution of the main shock without including potential displacements from several days to weeks of postseismic afterslip. The coseismic slip distribution indeed includes some contribution from the first 11 h of afterslip when GPS shows several centimeters of displacements (~3–4 cm of eastward motion at station PFRJ). However, this imaging aperture provides a nearly idealized opportunity to discriminate coseismic and postseismic displacements with a spatially dense data set.

Individual interferograms were processed with the *Gamma Remote Sensing InSAR Software* (<http://www.gamma-rs.ch>) and precise orbits provided by the European Space Agency. A challenge of TOPS mode processing is obtaining proper image coregistration, given that there are steep phase gradients between image bursts in the radar azimuth direction. Generally, coregistration to better than 0.01 pixel is necessary to properly align the bursts. To achieve this level of precision, we undertook a three-part coregistration approach. First, we performed an initial coregistration between single-look complex (SLC) images using the precise orbits and the Shuttle Radar Topography Mission (SRTM) 90 m digital elevation model (DEM) to allow for estimation of terrain-induced pixel shifts [Farr *et al.*, 2007]. We then perform a second amplitude-based offset estimation on the SLCs to improve coregistration in the range direction. Last, we iteratively shifted the coregistration in the narrow swaths where bursts overlap by reducing the double-difference phase within these swaths. This was repeated until azimuth offsets were at the necessary precision. We removed topographic phase with the 90 m SRTM DEM and unwrapped interferometric phase with a minimum cost flow algorithm [Costantini, 1998; Chen and Zebker, 2001]. Lastly, we resampled each interferogram to a computationally manageable number of data points and estimated the covariance structure of each interferogram using a data resolution-based resampling method (Figure S2) [Lohman and Simons, 2005; Lohman and Barnhart, 2010].

2.3. Inversions for Fault Slip

We inverted the coseismic and postseismic static displacements from InSAR and GPS observations assuming spatially variable slip on the subduction zone interface and purely elastic deformation (Figure 4). We neglect viscoelastic relaxation as a significant contributor to our observed postseismic displacement signals for two reasons. First, we expect that surface displacements induced by early viscoelastic relaxation are small relative to those induced by afterslip, given the short postseismic temporal aperture of our observations. Second, our inversions are dominated by spatially dense InSAR observations, and the displacement signal apparent in these observations comprises a smaller spatial area than the coseismic deformation area (Figure 2). Viscoelastic relaxation is expected to encompass a region similar to or broader than the coseismic deformation area [e.g., Nur and Mavko, 1974; Pollitz *et al.*, 2006]. Nonetheless, it is likely that some contribution of early viscoelastic relaxation exists in our observations and may be incorrectly mapped as afterslip; we assume that this contribution is small compared to the larger afterslip signal. We also ruled out the influence of displacements from aftershocks because the largest aftershocks that are likely to produce a detectable InSAR signature consistent with the spatial extent of our observations occurred before the first postevent InSAR acquisition. We explored the possibility that observed postseismic displacements were caused by aseismic slip on upper plate splay faults by conducting a suite of inversions that allowed for all possible fault slip geometries and slip directions using the Neighbourhood Algorithm [Sambridge, 1999]. Slip on a shallowly dipping plane consistent with the megathrust was the only fault model geometry that fit GPS observations and ascending and descending interferograms; thus, we infer that postseismic displacements are dominated by afterslip on the subduction zone megathrust.

We inverted both coseismic and postseismic static displacements for finite fault slip on a planar fault geometry approximated from the Slab1.0 subduction zone geometry [Hayes *et al.*, 2012]. For the coseismic slip distributions, we only inverted interferograms from the descending track so as to minimize the inclusion of early afterslip (Table S2). We used an iterative approach that variably resizes fault slip patches according to the model resolution (i.e., smaller patches where finer detail can be resolved and larger patches where only coarse detail can be resolved) [Barnhart and Lohman, 2010]. For the Illapel event, this procedure results in a model geometry consisting of 444 patches. For the coseismic inversion, we allowed slip direction (rake) to vary freely. The

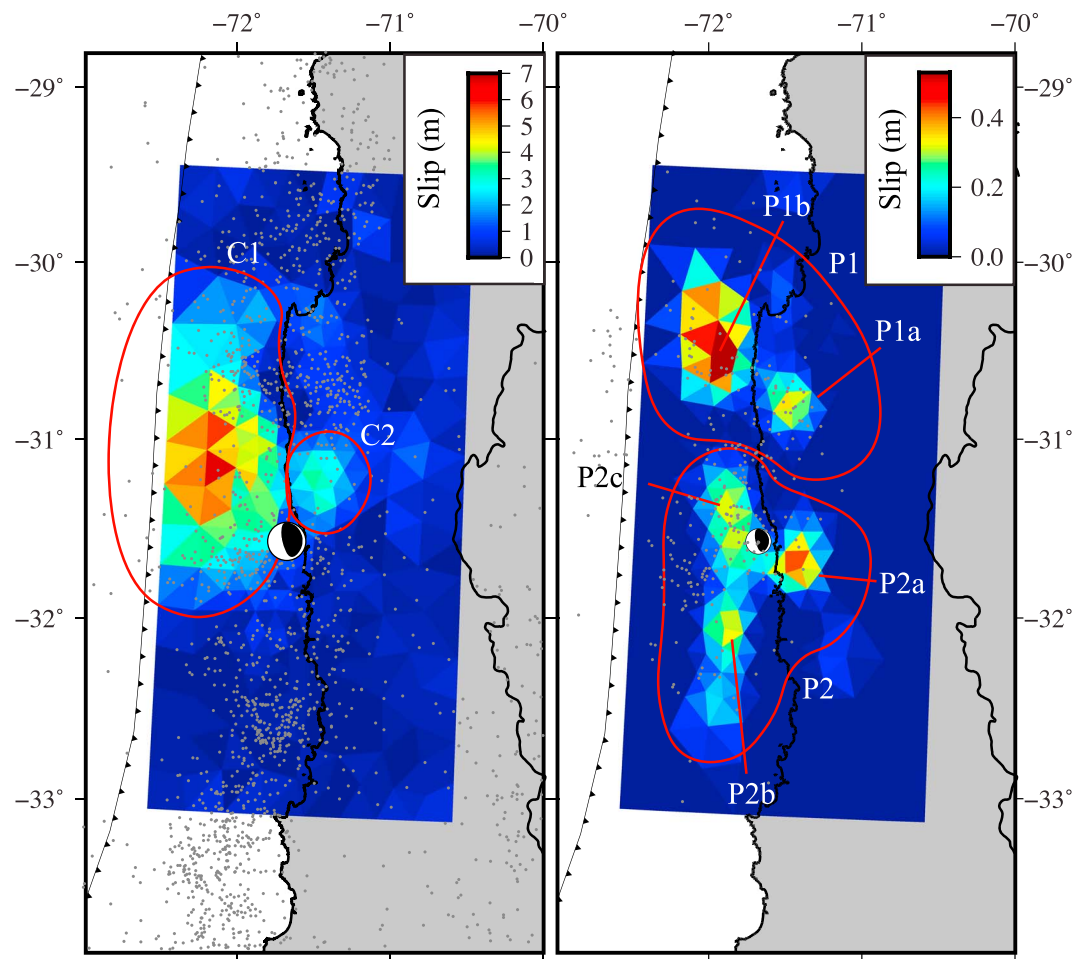


Figure 4. (a) Coseismic and (b) afterslip (first 26 days) slip distributions inferred from geodetic displacements. Specific regions are denoted for clarity of description in the text. The slip distributions shown are the median slip distributions from our Monte Carlo simulation. The full range of slip values is shown; however, only slip values >8 cm are interpreted. Model misfits are shown in Figure S2, and the 16th and 84th percentiles of the coseismic and afterslip (1–26 and 1–38 days) are shown in Figure S3. The gray dots in Figure 4a show the locations of earthquakes $>M_w$ 4.5 that occurred prior to the Illapel earthquake (1906, September 2015), and the gray dots in Figure 4b show the locations of aftershocks $>M_w$ 4.5 that occurred between 16 September 2015 and 15 October 2015 (USGS NEIC, www.earthquake.usgs.gov).

postseismic displacements are of smaller magnitude and are susceptible to trade-offs between slip direction and slip magnitude. To address the impact of these trade-offs, we inverted the GPS displacements alone for the best fitting single fault patch with uniform slip and then imposed this fixed slip direction (rake = 95°) on the distributed slip inversion. The inferred afterslip direction varies only 2° from the mean coseismic slip direction (rake = 97°). We used this approach to invert for postseismic afterslip at intervals of 26 and 38 days following the earthquake. Because inverting for spatially variable slip is an underdetermined problem, all inversions were regularized to avoid overfitting noise in the data with minimum moment regularization and a regularization constant chosen with the J_R criterion [Barnhart and Lohman, 2010]. In both coseismic and afterslip inversions, we did not apply relative weights to the GPS and InSAR observations. Instead, we weighted the Green's functions and data by the Cholesky factorization of the data covariance matrix so that the weighted data has uniform, unit variance [e.g., Harris and Segall, 1987; Barnhart and Lohman, 2010]. This grants greater weight to data with lower uncertainties (GPS); however, in practice, the fault slip distributions are dominated by the spatially dense InSAR observations that provide better model resolution. Model residuals are shown in Figure S2.

2.4. Fault Slip Uncertainties

One well-known limitation of fault slip inversions in subduction zone environments is that onshore geodetic observations have limited slip resolution on portions of the megathrust far from shore (i.e., near the trench).

Melgar et al. [2016] demonstrated that static geodetic displacements alone cannot uniquely resolve coseismic slip near the trench for the Illapel earthquake, and any inferred slip at the trench is likely regularization dependent. This limitation is also a factor for our inversions of postseismic afterslip, and uncertainties are further amplified by the presence of spatially coherent atmospheric noise in interferograms (Figure 2). To address these issues, we undertook two approaches to quantify the extent to which inverted slip might be biased by atmospheric noise. First, we jointly inverted two preseismic ascending and descending interferograms (containing no known deformation signals) for slip using the same inversion methodology and regularization described previously (Table S2). We found that up to 8 cm of slip was mapped onto the megathrust offshore. Accordingly, we refrain from interpreting any slip magnitudes <10 cm in our inversions as a means to be conservative in our interpretations of coseismic and afterslip overlap.

Second, we undertook a Monte Carlo error propagation approach to estimate the population of slip distributions that are consistent with available observations, given our knowledge of noise within these data sets [Barnhart and Lohman, 2013]. We added 500 realizations of synthetic noise with the same covariance structure of the resampled interferograms and GPS to the predicted displacements of the best fitting slip distributions. We then inverted each synthetic noisy data set for fault slip. We extracted the median slip distribution as our preferred model from these populations of slip distributions. Because regularization and nonnegative slip constraints are imposed, the statistical distribution is non-Gaussian. Thus, we define the 16th–84th percentiles of slip for each patch as the 68% confidence interval (Figure S3). All slip distributions illustrated and interpreted in this study are the median slip distributions from these Monte Carlo simulations. While the above measures account for uncertainty due to observational noise, we acknowledge that additional epistemic uncertainty remains due to several of our simplified assumptions that are common in fault slip modeling (e.g., Earth structure and fault geometry).

3. Results

3.1. Coseismic Slip

Coseismic displacements are broadly consistent with the expected displacement pattern of subduction zone earthquakes that primarily slipped offshore: dominantly trenchward displacements with broad-scale subsidence (Figure 2a). Additional GPS observations and interferograms decomposed into three-dimensional displacements that are not used in this study show that portions of the Chilean coastline uplifted coseismically [Grandin et al., 2016]. Coastal uplift is predicted if some coseismic slip propagated downdip of the coastline, as is inferred to have happened in the 2007 Tocopilla earthquake and the M_w 7.7 aftershock of the 2015 Iquique earthquake [Delouis et al., 2009; Motagh et al., 2010; Hayes et al., 2014].

Our coseismic slip distribution is consistent with other published slip distributions [Melgar et al., 2016; Tilmann et al., 2016] and the USGS National Earthquake Information Center's (NEIC) teleseismic finite fault slip solution (Figures 4a and S4). Together, these models suggest that slip propagated trenchward, with peak slip magnitudes of 6.5–6.7 m (C1; Figure 4a). The geodetically inferred magnitude from our inversions is M_w 8.24. One notable region of coseismic slip propagated downdip of the hypocenter beneath the Chilean coastline (C2; Figure 4a). This feature, with slip up to 3 m, is also apparent in kinematic slip distributions (USGS NEIC) [Melgar et al., 2016]. The consistency among slip distributions (Figure S4), the observation of coastal uplift consistent with slip downdip of the coastline [Grandin et al., 2016], and the model resolution afforded by geodetic observations in this portion of the rupture suggest that this region of downdip slip is a robust feature of the coseismic rupture. Given that this feature also appears in teleseismic and high-rate GPS source models, we conclude that this slip feature is not related to immediate postseismic slip, large aftershocks that occurred within hours of the main shock, or artifacts introduced by the static geodetic observations.

We map slip that propagates to the trench, consistent with the inference of rupture to the trench suggested by the resulting tsunami. However, as mentioned previously, the magnitude and spatial extent of slip that reached the trench cannot be uniquely determined with our observations. Slip inversions that include time-variable displacements (high-rate GPS and seismic waveforms; USGS NEIC [Melgar et al., 2016]) map larger magnitude slip near the trench than seen in our results, and we conclude that this discrepancy arises from the different observations and inversion strategies used among studies. Our coseismic slip inversions systematically underestimate the earthquake magnitude (M_w 8.24 versus M_w 8.3), which suggests that we are not able to resolve larger slip values near the trench. Our inversions also produce a coherent residual along

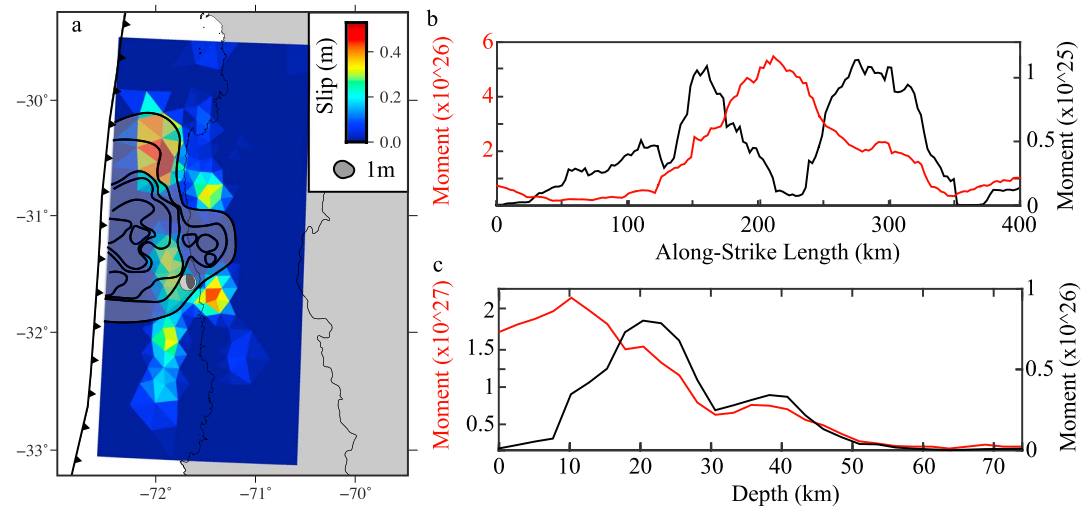


Figure 5. Spatial overlap of coseismic slip and early afterslip (first 26 days). (a) The afterslip distribution overlain by smoothed contours of coseismic slip. (b) Distribution of along-strike coseismic moment release (red) and afterslip moment release (black). (c) Distribution of down-dip coseismic moment release (red) and afterslip moment release (black). Note the difference in vertical scales between coseismic and afterslip moment in Figures 5b and 5c.

the coast of up to 10 cm in the radar line of sight (Figure S2). We have tested a range of possible models to explain it (slip on a splay fault, different regularization, and more complex fault geometries), but none of these scenarios are able to reconcile both InSAR and GPS observations. GPS station PFRJ is located within this region of misfit (Figure 2a). Our median slip distribution fits horizontal GPS offsets well, but it overestimates the recorded subsidence by 7 cm (Figure S2a). This misfit indicates that we map slip into our inversion, likely offshore, that overpredicts coastal subsidence (34 cm modeled versus 24 cm of recorded subsidence; Figure S2). Postseismic motion during the first 11 h after the main shock, present in the InSAR data but not the GPS, could also contribute to an overestimate of coseismic slip.

3.2. Afterslip

Continuous GPS stations recorded immediate onset of time-variable postseismic displacements following the earthquake that continued throughout our observation period (see 5 min kinematic point position solutions at http://earthquake.usgs.gov/monitoring/gps/Chile_2015/; Figures 3 and S1). The displacements generally followed the directional pattern of coseismic displacements, with dominantly westward motions indicative of continued slip on the megathrust and a slip orientation similar to that of the main shock (Figure 2b). Three coastal stations south of the epicenter exhibited a different sense of motion compared to their coseismic offsets, suggesting that slip changed location (LVIL, PFRJ, and ZAPA; Figures 2b and S1). LVIL changed direction from coseismic northward motion and subsidence to postseismic southward motion and uplift. ZAPA likewise changed from undetectable coseismic displacement to resolvable postseismic northwest motion and subsidence (Figures 2b and S1). Coastal station PFRJ exhibits negligible postseismic vertical displacements in the first 36 days, following the earthquake despite recording a peak coseismic subsidence of 24 cm.

Postseismic imagery acquired immediately following the earthquake likewise resolves surface displacements along the Chilean coast, particularly in track 156 (beginning 17 September 2015; Figure 2b). Interferograms show two lobes of line-of-sight (LOS) shortening (uplift/eastward motion) along the Chilean coast that have an opposite sense of motion from coseismic interferograms and a lobe of LOS lengthening (subsidence/westward motion; Figures 2b and S2). A broader region of subsidence, apparent in interferograms and GPS-recorded vertical displacements, surrounds these three lobes. Postseismic uplift recorded at LVIL is co-located with the southernmost lobe of LOS shortening apparent in the postseismic interferogram (Figures 2b and S2).

Figure 4b shows the spatial distribution of inferred afterslip from 17 September 2015 to 15 October 2015 (26 days). Two distinct lobes of slip (P1 and P2; Figure 4b) are apparent that bracket both the large (C1) and smaller down-dip (C2) regions of coseismic slip along-strike. Peak mapped afterslip reaches ~52 cm,

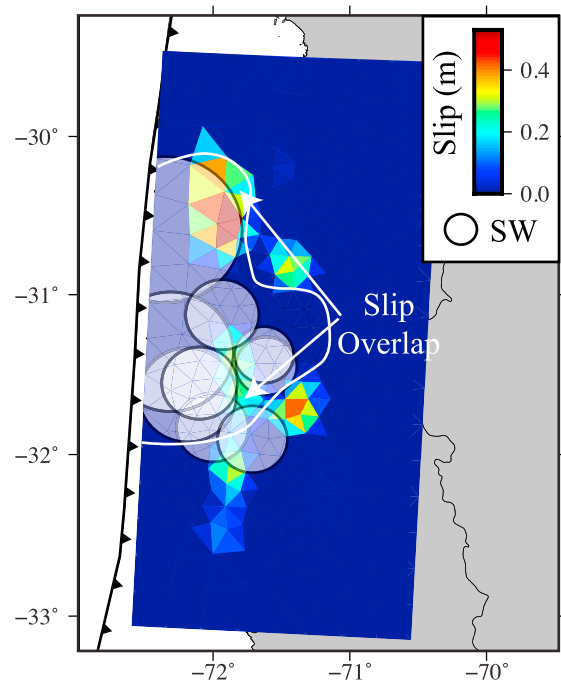


Figure 6. Slip resolution test overlay on the postseismic slip distribution. The circles represent the smoothing area of single-fault slip patches in the coseismic slip distribution that do not overlap with afterslip locations. The radius of each circle is the smoothing radius of each slip patch. The circles that overlap with afterslip patches reflect regions where the slip inversions cannot discriminate if slip styles truly overlap. The white outline reflects the approximate extent of coseismic slip. Afterslip regions that fall within this outline and are not spanned by the smoothing areas represent the regions where coseismic slip and afterslip overlap is resolved by the inversion (denoted in the figure). For simplicity, we have only shown the smoothing widths that account for the greatest overlap with afterslip regions, and we have only plotted afterslip >8 cm (patches with slip <8 cm have been assigned 0 m slip).

characteristics in our models of early afterslip following the Illapel earthquake and describe them in further detail below:

1. Inferred coseismic slip and afterslip overlap substantially (Figure 5), but interpretation of this result is limited given the resolving power of the available data (Figure 6);
2. Afterslip occupies regions of the megathrust along-strike from the coseismic rupture, and afterslip does not extend downdip of the deepest region of coseismic slip (Figure 5);
3. Afterslip occurs across a broad range of inferred interseismic coupling values (50–100% coupled) rather than preferentially occurring in areas of lower coupling (Figures 7 and 8).

4.1. Spatial Distribution of Coseismic Slip and Afterslip

Early afterslip following the Illapel earthquake occurs in two regions that overlap with, and extend along-strike from, the northern and southern extents of coseismic slip (P1 and P2; Figures 4 and 5). Broadly, downdip afterslip (P1a and P2a; Figure 4b) brackets deep coseismic slip (region C2) along-strike with little spatial overlap (Figures 4 and 5). A southern region of afterslip (P2b) likewise brackets coseismic slip along-strike (Figures 4 and 5). Altogether, afterslip occurs at depth ranges similar to the coseismic rupture (Figure 5c). The existence of along-strike afterslip following the Illapel earthquake, as opposed to solely downdip afterslip, was also inferred to have occurred following the 2010 Maule and 1995 Antofagasta earthquakes [Pritchard and Simons, 2006; Lin et al., 2013; Bedford et al., 2013]. Our slip distributions also map two regions of afterslip that appear to overlap substantially with mapped coseismic slip (P1b and P2c; Figures 4b and 5). This result contradicts the hypothesis that slip behavior of the subduction interface is strictly partitioned

and the cumulative aseismic moment release over the 26 days following the earthquake is M_w 7.4 ($+0.2/-0.1$), which is approximately 2% of the teleseismically inferred seismic moment of the main shock. Aftershock activity cataloged by the USGS within this time period only accounts for ~19% of the afterslip moment release we have inferred. Inversions of postseismic displacements spanning the first 38 days following the earthquake show a similar spatial pattern of slip with a small but expected increase in cumulative moment ($\sim M_w$ 7.5, $+0.2/-0.1$) and slightly more trenchward slip in the southern lobe (P2) of slip (Figure S3). Two regions of afterslip (P1a and P2a; Figure 4) bound the deepest extent of coseismic slip along-strike (~ 55 km, C2) and extend to approximately the same depth as the coseismic slip (Figure 5). We do not find evidence that afterslip fills unruptured portions of the megathrust immediately downdip of the deepest coseismic slip (Figure 5).

4. Discussion

Our mapped distributions of coseismic slip and afterslip provide means to characterize potential overlap between slip styles and their relationship to interseismic coupling. We identify three general

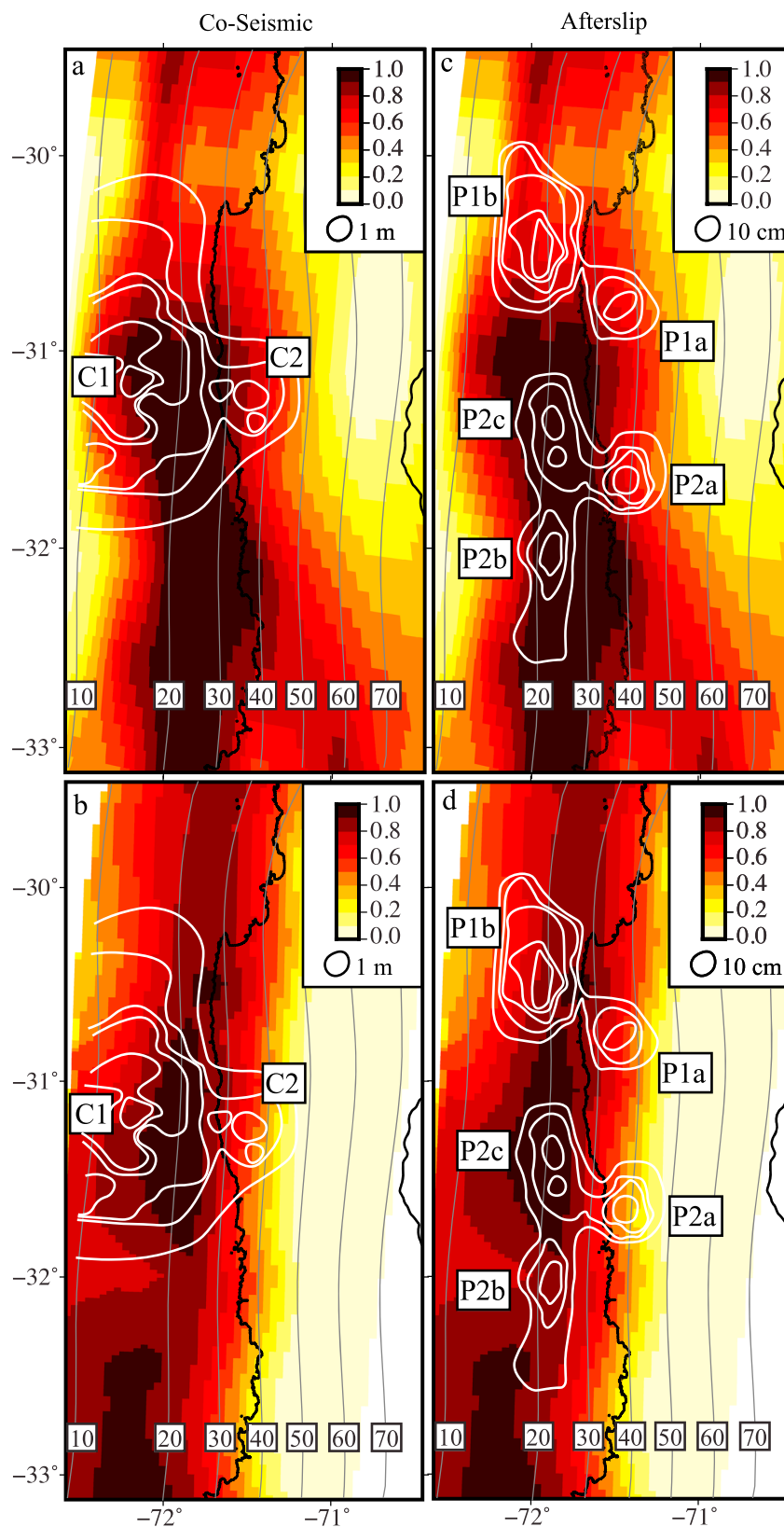


Figure 7. Smoothed contours of (a and b) coseismic slip and (c and d) afterslip overlain on the interseismic coupling models of Métois *et al.* [2012] (Figures 7a and 7c) and Tilmann *et al.* [2016] (Figures 7b and 7d). Slip regions are denoted as in Figure 4 for description clarity. Depth contours (km) of the subducting slab are shown in dark gray [Hayes *et al.*, 2012].

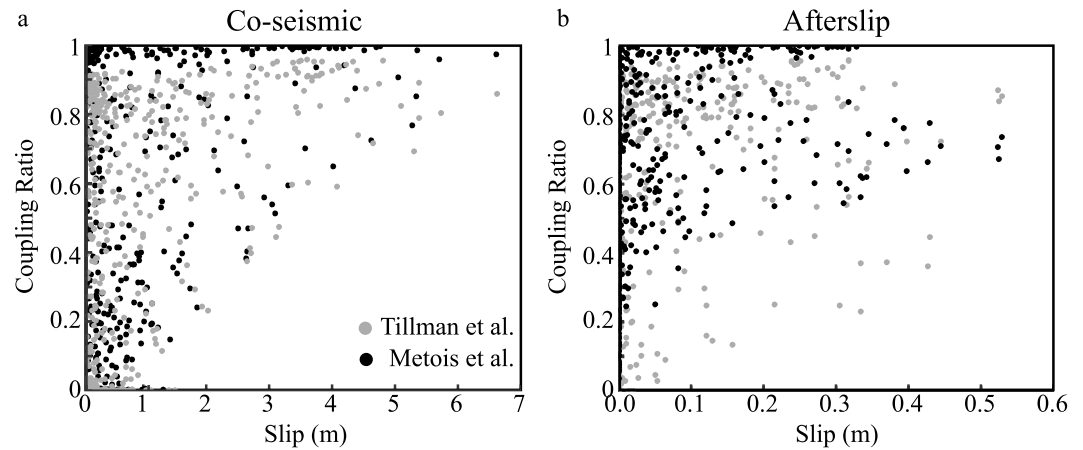


Figure 8. (a) Relationship between coseismic slip and interseismic coupling ratio. (b) Relationship between afterslip (first 26 days) and interseismic coupling. For each fault slip patch in Figure 3, a coupling ratio is calculated by finding the average coupling of all mapped dislocation from Métois et al. [2012] and Tillmann et al. [2016] that lay within the fault slip patch.

between stick-slip asperities and creeping zones. Overlapping coseismic slip and afterslip were likewise inferred for the Maule and Antofagasta earthquakes [Pritchard and Simons, 2006; Bedford et al., 2013; Lin et al., 2013].

One important consideration with respect to our finite fault slip inversions is the degree to which we can resolve spatial overlap between coseismic slip and afterslip versus apparent overlap introduced by inversion regularization. This is especially pertinent in offshore slip regions where we map substantial slip overlap yet resolution is expected to be poor (i.e., regions P1b and P2c; Figures 4 and 5). Our Monte Carlo tests provide a sense of slip variability that may be introduced by atmospheric noise; however, they do not explicitly address the resolution of the fault slip inversions. To gain a first-order sense of slip resolution, we consider the model resolution matrix (R_m) of our co-cure 6) [e.g., Barnhart and Lohman, 2010]:

$$R_m = G^{-g}G \quad (1)$$

$$G^{-g} = \left(\begin{bmatrix} G \\ \lambda L \end{bmatrix}^T \times \begin{bmatrix} G \\ \lambda L \end{bmatrix} \right)^{-1} G^T \quad (2)$$

where G is the elastic Green's function computed from the distribution of data points and fault slip dislocations [Meade, 2007], L is the regularization matrix, and λ is the regularization coefficient chosen using the β_1 criterion. Superscripts T and -1 indicate the matrix transpose and inverse, respectively. The model resolution matrix provides a metric to describe the distance over which unit slip at a single point is smoothed onto the surrounding fault surface region, and it is a function of both the experimental design (data locations and uncertainties and slip patches) and the imposed regularization [Du et al., 1992; Barnhart and Lohman, 2010]. We refer to this distance as the smoothing radius, and it measures the length scale over which unit slip can be resolved within 1 sigma uncertainties [Barnhart and Lohman, 2010]. The variable resampling algorithm that we use mitigates these effects, but it does not completely remove them since we impose regularization to account for nonuniqueness of the inverse problem introduced by noise, limited model resolution, and simplification of the fault geometry and elastic structure [Barnhart and Lohman, 2010]. This method, combined with the Monte Carlo error analysis, provides a generalized means to test the robustness of certain slip features, as others have explored through checkerboard tests or comparing data misfits when slip is constrained to only certain portions of the subduction interface [e.g., Hsu et al., 2009].

We examine coseismic fault slip patches that are adjacent to, but do not overlap with, afterslip. We then plot the smoothing radii of these patches (Figure 6). In this test, if smoothing radii alone from coseismic slip patches span the entire region of coseismic/afterslip overlap, then we cannot determine if slip styles indeed overlap. Otherwise, we can infer that our slip distributions require that coseismic and afterslip patches overlap. This in turn would suggest that actual coseismic slip and afterslip (slip that physically occurred in this sequence and that we are attempting to image) can occur in the same locations.

From this test, we find that there are certain regions where slip overlap between models is required by the observations in the northernmost extent of region P1b and the southernmost region of P2c (denoted in Figure 6). In turn, we infer that some degree of actual slip overlap likely occurred. Beyond these small regions, nearly all of the overlapping afterslip and coseismic slip fall within smoothing radii of the coseismic slip patches. This indicates that the vast majority of the spatial overlap we report can be potentially explained exclusively by the resolution limitations of our inverse problem that are governed by the location and quality of data relative to fault slip patches and imposed regularization (Figure 6). Thus, we cannot state conclusively that slip styles physically overlap as presented in Figure 5a. This does not rule out the possibility of overlapping coseismic slip and afterslip within regions where coseismic slip smears into afterslip regions. Rather, it shows that the available observations do not have sufficient spatial resolution to definitively image truly overlapping slip areas.

In either case though, the fault slip distributions point toward unexpected slip style interactions that have important consequences for megathrust fault behavior. If coseismic slip and afterslip indeed overlap substantially, then simple velocity-weakening and velocity-strengthening descriptions may be inconsequential within a single earthquake sequence. Conversely, if slip styles overlap minimally or not at all, then the frictional properties of the megathrust are highly heterogeneous both along-strike and down-dip.

4.2. Fault Slip and Interseismic Coupling

We compare our distributed slip inversions to two separate estimates of interseismic coupling based on GPS velocities (Figures 7 and 8) [Tilman et al., 2016; Métois et al., 2012]. High interseismic coupling has been shown to correlate well with the rupture areas of subsequent large earthquakes in multiple subduction zones [e.g., Konca et al., 2008; Moreno et al., 2010; Loveless and Meade, 2011; Hayes et al., 2014]. Kaneko et al. [2010] hypothesized from dynamic rupture models that spatial variations in interseismic coupling correspond to variations in the frictional properties of the fault (i.e., rate strengthening versus rate weakening). In this framework, coseismic rupture is expected to happen in regions of high interseismic coupling, while regions of partial coupling indicative of rate-strengthening friction would arrest rupture and host afterslip.

In the Illapel earthquake, we observe that coseismic slip predominantly occurred within regions of high interseismic coupling (Figures 7a, 7b, and 8a) [Métois et al., 2012, 2016; Tilman et al., 2016]. Moreover, we observe an apparent correlation between inferred interseismic coupling ratio and maximum coseismic slip (Figure 8a). The largest slip magnitudes occur only in the areas with the largest coupling ratios, and regions of lower coupling only exhibit small amounts of slip (Figure 8a). There is no apparent relationship between coupling ratio and minimum coseismic slip. For example, areas of high coupling are found to encompass a range of slip magnitudes (Figure 8a). However, further interpretation of this pattern is difficult since it is likely that regularization of both our slip and the published coupling inversions may partially account for low-amplitude slip inferred on poorly resolved portions of the fault far from the coast. We note too that coseismic slip did not continue southward into a laterally continuous region of high coupling apparent in the interseismic model of Métois et al. [2012] (Figure 7a), as might be expected if coupling is a direct corollary for frictional state and no preexisting stress heterogeneities exist [Kaneko et al., 2010]. The coupling model of Tilman et al. [2016] (Figure 7b) shows a small region of lower interseismic coupling (~ 0.7) in this region that may explain rupture termination.

Afterslip exhibits a more nuanced spatial correlation to interseismic coupling than coseismic slip, owing in part to differences between the coupling models of Métois et al. [2012] and Tilman et al. [2016] (Figures 7c, 7d, and 8b). Generally, we find that afterslip follows a relationship that is similar to coseismic slip, where maximum afterslip magnitude increases with increasing preseismic coupling ratio (Figure 8b). This relationship is more distinct with the Métois et al. [2012] model but is consistent with both. We also observe that afterslip occurs across a broad range of coupling ratios, including in regions with apparently high coupling (80–100%; Figures 7c, 7d, and 8b).

The northern lobe of shallow afterslip (region P1b) occurs in a region where coupling is inferred to decrease to ~ 45 – 75% (Figures 7c and 7d). This is consistent with the expectation that afterslip should occur in regions of rate-strengthening frictional behavior that may be highlighted by both lower interseismic coupling and coseismic rupture termination [Kaneko et al., 2010]. While afterslip region P2 extends southward along-strike from the southern termination of coseismic slip (Figure 5a), it occurs in regions of high interseismic coupling

(80–100%; Figures 7c and 7d). Deep afterslip in both the northern and southern lobes (regions P1a and P2a) extends into regions of lower coupling at ~30–50 km depths (down to ~45% coupling) but terminates at a similar depth and within similar coupling conditions as coseismic rupture. These findings suggest that both coseismic slip and afterslip extended to the stable-sliding region of the megathrust.

4.3. Frictional Properties of the Subduction Megathrust

A simple interpretation of rate and state friction would dictate that coseismic slip must be confined to rate-weakening regions, characterized by full interseismic locking, and afterslip to velocity-strengthening zones typically located updip and downdip of the locked zone. In contrast, our results for the Illapel earthquake suggest that coseismic slip and afterslip overlap, and no appreciable afterslip occurs downdip of the main shock rupture area. If afterslip can only occur under rate-strengthening conditions, the overlap implies that coseismic slip must have propagated significantly beyond the spatial bounds of rate-weakening asperities, perhaps including rupture onto the deeper portion of the subduction interface at depths of 30 km–60 km, which may be a transitional zone from fully locked to creeping areas. Furthermore, our models show both the apparent arrest of coseismic slip and the subsequent occurrence of afterslip around 32°S within a zone of high interseismic coupling (80–100%) that is imaged in two different coupling models (Figures 7c, 7d, and 8a) [Métóis *et al.*, 2012; Tilmann *et al.*, 2016]. While the spatial details of coseismic slip, afterslip, and interseismic coupling remain uncertain due to the limited resolution afforded by available data, our results provide further evidence for complex fault slip behavior arising from the interplay of fault frictional properties, pore fluids, premain shock stress conditions, and other factors as discussed in the following paragraphs.

It has long been recognized that coseismic slip could propagate into velocity-strengthening regions, where the ensuing negative stress drop would arrest rupture [Marone *et al.*, 1991]. Tse and Rice [1986] and Kato [2007] used numerical simulations to demonstrate that coseismic slip could penetrate into velocity-strengthening areas of the fault that are characterized by positive but small $\sigma_n(a - b)$, where σ_n is the effective normal stress. Within the velocity-strengthening region, the lower the value of $\sigma_n(a - b)$ is, the farther coseismic slip can propagate, the farther afterslip will extend from the terminus of coseismic slip, and the more quickly afterslip will decay. Lin *et al.* [2013] suggested that a large zone of low, positive $\sigma_n(a - b)$ beneath the Arauco Peninsula acted as a rupture barrier during the Maule earthquake and could reconcile apparently overlapping coseismic and postseismic slip. Furthermore, Johnson *et al.* [2016] conclude that only 25% of the coseismic slip area inferred from seismic source inversions for moderate to large earthquakes on the northern Japan subduction zone from 2003 to 2011 is fully locked during the interseismic period, implying that coseismic rupture extends beyond the boundaries of locked asperities. Noda and Lapusta [2013] demonstrated that on strike-slip faults under certain conditions coseismic slip not only could propagate into a velocity-strengthening region but also might initiate sustained unstable slip in that region, thus leading to larger coseismic ruptures than would be expected from the spatial distribution of inferred interseismic locking. Their study focused on thermal pressurization of pore fluids due to shear heating; however, other weakening mechanisms could produce a similar effect. Whether similar processes might apply to downdip rupture propagation in subduction zones, where increasing temperature with depth would simultaneously accentuate velocity-strengthening frictional behavior and bring the fault zone closer to the brittle-ductile transition, is less clear. While we cannot pinpoint the particular fault zone properties or physical mechanism(s) applicable to the Illapel event, these studies provide examples of conditions capable of producing the overlapping coseismic and postseismic slip that we infer and the propagation of coseismic slip northward onto portions of the subduction interface not thought to be fully locked.

Several factors might account for the southern termination of coseismic slip and the ensuing afterslip in a zone of high coupling (Figure 7). Perhaps the simplest explanation is that the subduction interface at this location is, in fact, not strongly coupled. As highlighted by the differences between the two published coupling models shown in Figure 7, the limited ability of GPS to resolve earthquake-related slip and interseismic locking, as well as the influence of model regularization, introduces substantial uncertainty that is difficult to constrain. For example, Métóis *et al.* [2012] show that in our region of interest, the coupling ratio (on a scale of 0–1) averaged from 0–60 km depth has uncertainties up to approximately ± 0.06 . If individual fully locked asperities are of limited size, as suggested by Johnson *et al.* [2016], the attendant variations in subduction interface coupling might impact earthquake nucleation and propagation but are likely below the resolving power of the data. As discussed by Kaneko *et al.* [2010], preexisting stress conditions due to previous

earthquakes may also strongly influence the location, timing, and size of future coseismic ruptures. Further highlighting the complexities controlling fault slip, the simulations carried out by *Noda and Lapusta* [2013] showed that velocity-strengthening regions that occasionally participate in large events can appear either locked or creeping at different times during the interseismic period. *Helmstetter and Shaw* [2009] argue that afterslip cannot be adequately modeled using a steady state friction law and that evolving stress conditions can give rise to afterslip even where the fault surface is velocity weakening.

4.4. Other Possible Factors Influencing Slip

There are several additional factors that may influence the coseismic rupture extent, spatial relationship between fault locking and earthquake-related slip, and the conclusions to be drawn from the geodetic observations presented here.

First, we compare coseismic and afterslip distributions to interseismic coupling models derived from GPS observations acquired prior to the 2010 Maule earthquake, which occurred south of the Illapel earthquake. Accordingly, these interseismic coupling estimates may not accurately reflect coupling of the plate interface from 2010 to 2015. Moreover, published interseismic coupling models, such as those we interpret in this paper, are derived from varying suites of observations and implement a range of different modeling assumptions. Together, these factors can lead to apparent inconsistencies between coupling models despite comparable data agreement. Variation among different models provides some insight into the associated epistemic uncertainty, and common features may be more robust. Nevertheless, care should be taken in directly interpreting the features of both coupling and slip models.

We have not taken into account the possible role of pore fluid pressure on the subduction zone megathrust. High pore pressure could provide one explanation for afterslip in a region of apparently high coupling, and it could be either an intrinsic property of the system evidenced by critical wedge theory and regional geology [*Cubas et al.*, 2013] or a continuing transient process induced by the Maule earthquake. Postseismic deformation from the Maule earthquake could also contribute to stress heterogeneity. As described previously, we have also explicitly neglected the potential contributions of viscoelastic relaxation that may be incorrectly mapped as fault slip. Thus, the observed afterslip pattern may reflect the influence of several stressing sources.

We have not accounted for the potential impacts of the 1943 earthquake that is inferred to have ruptured a similar part of the subduction zone as the Illapel earthquake (Figure 1) [*Beck et al.*, 1998]. While the spatial extent of this earthquake is poorly known, it could potentially introduce a continuing stress heterogeneity that promotes the spatial relationships we observe. We find this scenario to be unlikely, given that coupling models are derived entirely from observations after the 1943 earthquake, but we cannot discount it entirely.

Lastly, we have not accounted for the potential thermal, pore pressure, or topographic effects of the subducted Juan Fernandez Ridge (JFR; Figure 1). *Sparkes et al.* [2010] noted that the JFR coincides with the northern termination of rupture in the 2010 Maule earthquake and the southern termination of the 1943 earthquake. These authors conclude that in most cases subducted ridges act as rupture barriers by reducing subduction interface coupling, as evidenced by little observed background seismicity. However, in the vicinity of the JFR there is substantial background seismicity, leading Sparkes et al. to suggest that other factors counteract the weakening effect of ridge subduction to produce a strongly coupled barrier to rupture propagation. If the JFR demarks the southern terminus of coseismic slip in the Illapel event, our results imply that afterslip must overlap with, or even cross, the subducted ridge.

4.5. Coastal Uplift

A second intriguing characteristic of this earthquake sequence is the occurrence of coastal uplift that is induced by both coseismic slip and afterslip that propagated downdip of the Chilean coastline to depths of 30–45 km (Figure 5; herein termed “deep” slip). In typical great subduction ruptures, coseismic subsidence of the adjacent continental coastline is observed [e.g., *Plafker and Savage*, 1970]. Figure 9 shows the pattern of uplift and subsidence predicted by our coseismic and afterslip models. Coseismic coastal uplift (within 15–25 km of the coastline) is independently confirmed by observations from GPS and three-dimensional decompositions of Sentinel-1a interferograms [*Grandin et al.*, 2016], while postseismic uplift is confirmed by our GPS observations (Figures 9 and S1). The magnitude and loci of predicted coseismic uplift regions, with peak uplift of ~20 cm, are also consistent with uplift deduced by *Grandin et al.* [2016] from Sentinel-1a imagery.

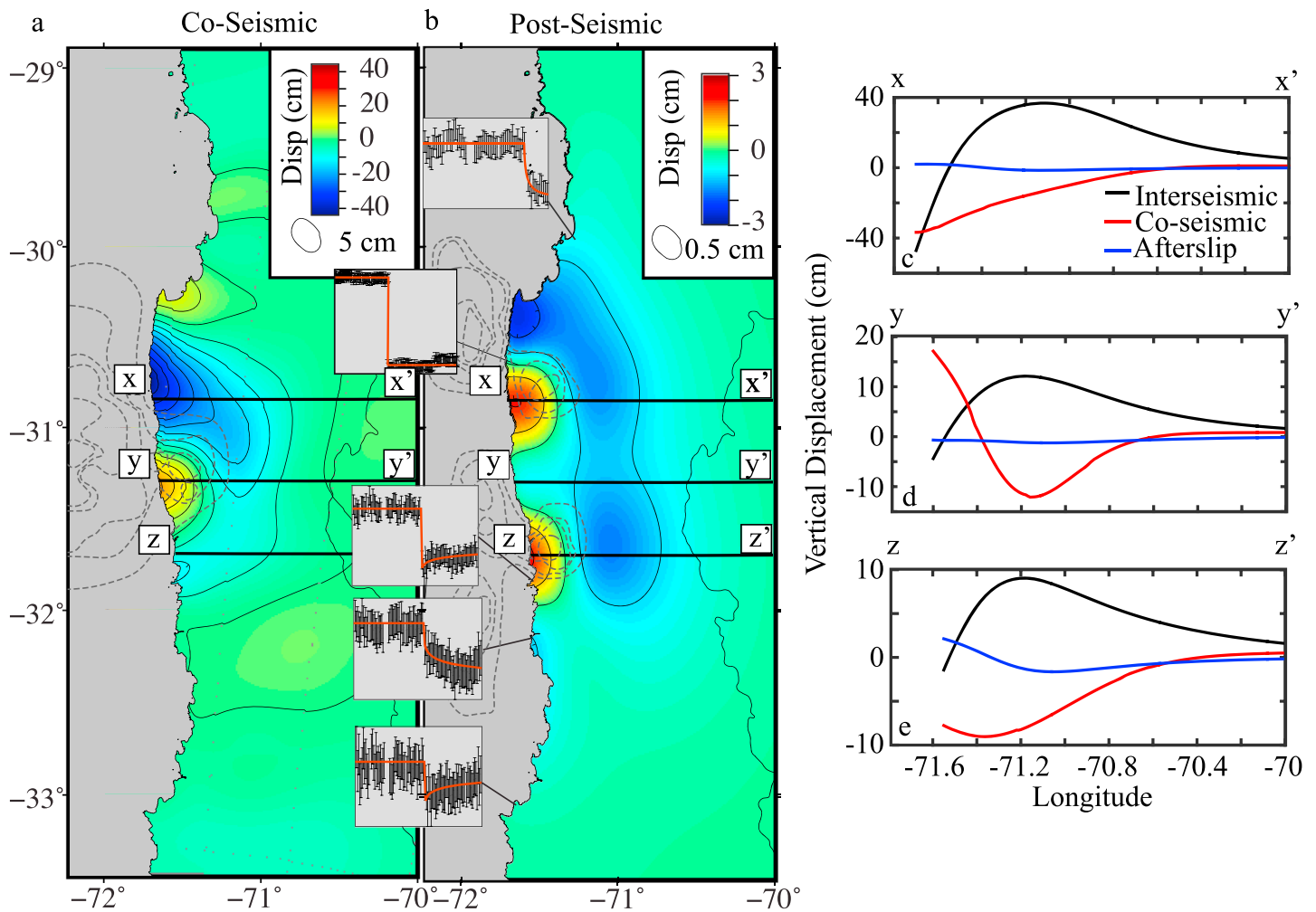


Figure 9. Vertical displacements inferred from the (a) coseismic and (b) postseismic slip distributions (first 26 days). Coastal GPS time series are shown, which corroborate the inferred vertical displacement direction. Contours of coseismic slip and early afterslip are shown as dashed gray contours, and contours of vertical displacement are shown as black contours. The profiles extending from the coastline (x - x' , y - y' , and z - z') show the predicted coseismic (red) and postseismic (blue) vertical displacements. The predicted interseismic vertical displacements, where the magnitude of interseismic maximum uplift is scaled to the maximum coseismic subsidence in each profile, are plotted in black.

Our slip distribution predicts that maximum coseismic subsidence of ~ 40 cm occurs adjacent to the region of the coseismic uplift (Figure 9a). The lack of substantial residuals in our postseismic inversions indicates that we have likely characterized postseismic uplift well while overestimating coastal coseismic subsidence (Figure S2). Postseismic coastal uplift of up to ~ 3 cm generated by early afterslip is overprinted on both coseismic uplift and subsidence, as illustrated by profiles of the distribution and magnitudes of coseismic and postseismic uplift (x - x' , y - y' , and z - z' ; Figure 9).

The occurrence of coseismic coastal uplift generated by slip downdip of the coastline places the Illapel in a growing class of similar earthquakes that have also ruptured along the South American subduction zone: the 1995 M_w 8.0 Antofagasta, 2007 M_w 7.7 Tocopilla, 2010 M_w 8.8 Maule, 2012 M_w 7.1 Constitución, and 2014 M_w 7.7 Iquique earthquakes [Ortlieb et al., 1996; Pritchard et al., 2002; Delouis et al., 2009; Motagh et al., 2010; Tong et al., 2010; Ruiz et al., 2013; Hayes et al., 2014]. In these earthquakes, coseismic slip likely straddles and extends downdip of the contact between the subducting slab and overriding continental Moho (~ 25 – 30 km depth in the vicinity of the Illapel earthquake [Lloyd et al., 2010]), indicating that these earthquakes propagate deeper than the elastic-crystal plastic transition of the overriding plate.

A long-standing question in subduction studies is what processes allow coastlines above subduction zones to gradually uplift at rates $\ll 1$ mm/yr over the span of multiple megathrust earthquake cycles. Upper plate

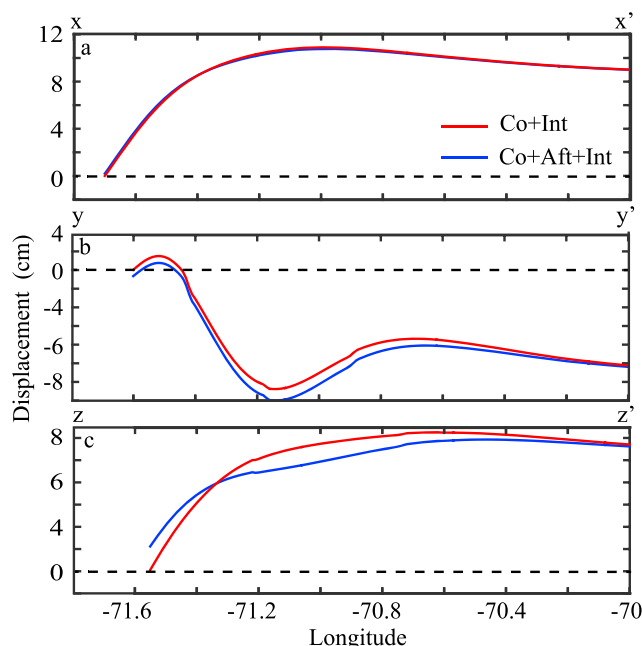


Figure 10. (a–c) Profiles of summed coseismic, interseismic, and early afterslip vertical displacements from Figure 9. Displacements are shifted such that summed coseismic and interseismic displacements are fixed to zero displacement at the coastline (dashed horizontal lines). In each case, the coseismic displacement pattern is not anticorrelated with the interseismic displacement pattern, thus leaving residual displacements. Furthermore, in cases where afterslip leads to coastal subsidence (y – y'), the magnitude of subsidence is insufficient to consume coseismic coastal uplift.

(black curves) profiles of the scaled interseismic deformation predicted by the coupling model of Métois *et al.* [2012]. In these profiles, we scale the predicted interseismic displacements to the maximum coseismic displacement in order to illustrate if coseismic deformation alone can completely consume interseismic deformation accrued late in the earthquake cycle. In Figure 10, we show the summed vertical displacement profiles of coseismic deformation, afterslip deformation, and scaled interseismic deformation (Figures 9c–9e). Generally, we observe that coseismic displacements and summed coseismic/afterslip displacements are not perfectly anticorrelated to interseismic displacements, resulting in net uplift along a narrow (~25 km) strip along the coast (Figure 10). This suggests that the Illapel sequence generated surface deformation that did not solely release presumably elastic interseismic strain. We also note that the locus of coseismic and interseismic deformation “peaks” are offset, which may be indicative of permanent coastal uplift [Sawai *et al.*, 2004].

Conversely, deep afterslip generated a corresponding broad region of subsidence landward of the narrow strip of coastal uplift (Figures 9 and 10b). If it is assumed that deep megathrust fault slip and afterslip produces permanent deformation, this region of subsidence should likewise be permanent, yet permanent subsidence is incompatible with the fact that the region is slowly uplifting. Furthermore, the mismatch between coseismic and interseismic displacements profiles may suggest that the Illapel earthquake was not a characteristic earthquake [Tilmann *et al.*, 2016]—a core assumption of the Melnick [2016] hypothesis. We acknowledge, though, that the coupling models only characterize coupling late in the earthquake cycle and do not account for temporal variations in fault coupling or viscoelastic effects [e.g., Wang *et al.*, 2012]. One possibility is that postseismic viscoelastic relaxation might reverse the apparent landward subsidence trough, as has been observed in Alaska after the 1964 rupture [Suito and Freymueller, 2009]. While the observed coastal uplift is consistent with the hypothesis that deep fault slip may contribute to permanent coastal uplift, incomplete knowledge of strain accumulation patterns throughout and across multiple earthquake cycles limits the extent to which we can attribute permanent coastal uplift to coseismic and postseismic uplift alone. Additionally, landward afterslip-induced subsidence, if not reversed in coming years by

(splay) faults, subducted sediment, bulk shortening in the interseismic interval, deep afterslip, and continuous and/or episodic fault creep have been proposed as drivers of permanent coastal uplift [Armijo and Thiele, 1990; Sawai *et al.*, 2004; Clift and Hartley, 2007; Contreras-Reyes *et al.*, 2012], but recent work by Melnick [2016] suggests that these processes alone do not account for the magnitudes and spatial patterns of geomorphically recorded uplift along the length of the Andean margin. Rather, Melnick [2016] proposes that megathrust earthquakes that propagate downdip of the Moho contact generate permanent uplift, given that they entail slip downdip of the elastic-crystal plastic transition.

In part, the Illapel sequence conforms to the hypothesis of Melnick [2016] that deep slip might correspond with zones of permanent uplift along the Chilean coast (Figure 9). However, afterslip also appears to contribute to coastal uplift during this event. To place coseismic and postseismic uplift in the context of the entire strain accumulation and release cycle, we show in Figures 9c–9e

viscoelastic deformation or deeper afterslip, may challenge the idea that afterslip alone is responsible for net, nonrecoverable coastal uplift adjacent to subduction zones and instead confirm that afterslip is simply a manifestation of elastic strain release.

5. Conclusions

The 2015 Illapel earthquake, like several recent earthquakes observed with dense geodetic observations, highlights the mechanical complexities that may exist on a subduction zone interface. The first-order characteristics of coseismic slip and early afterslip we infer add to the growing suite of observations that suggest the megathrust interface likely cannot be simply discretized into regions of stable and unstable slip. Rather, slip that is expected to correspond to just one of these different regimes (i.e., coseismic slip in an unstable, rate-weakening asperity) may propagate into adjacent regions where steady creep (i.e., afterslip) dominates. Furthermore, the Illapel earthquake sequence provides evidence that aseismic afterslip can propagate within regions of high interseismic coupling that are generally assumed to reflect rate-weakening frictional properties. This suggests that interseismic coupling may not be a direct proxy for velocity-weakening frictional properties. Instead, it may be better to conceptualize coupling ratios as a metric for asperity density averaged over a single model fault patch, where an individual asperity of some unknown dimensions is 100% coupled and all other regions are uncoupled as proposed by *Johnson et al.* [2016].

The Illapel sequence highlights the limitations of interpreting inverse models of offshore fault slip and interseismic coupling from onshore geodetic observations alone. We have shown that within the reasonable uncertainties of these slip inversions, fault slip occurring at different time intervals may appear to overlap spatially. Yet the inverse problem may be unable to definitively discriminate if coseismic slip and afterslip indeed overlap, given the limitations of the model resolution of the inverse problem itself. This issue is equally relevant to interseismic coupling models where sets of small, distributed, locked asperities may give the appearance of uniform locking in a necessarily regularized inversion [*Johnson et al.*, 2016]. Other inversion strategies, such as Bayesian or sparsity methods [*Yabuki and Matsu'ura*, 1992; *Evans and Meade*, 2012], may provide additional means to assess these spatial relationships. Model resolution tests and/or other approaches should be routinely employed to characterize the spatial scale of features that can be resolved by available observations. This information is critically important to allow proper use of model results as a starting point for follow-on studies and interpretations.

Long-term coastal stability and uplift adjacent to subduction zones imply that coseismic coastal subsidence, where observed, is reversed and becomes net uplift over multiple seismic cycles. Previous work has suggested that occasional deep coseismic ruptures and afterslip may generate permanent coastal uplift in places where elastic coseismic subsidence typically reverses interseismic uplift [e.g., *Sawai et al.*, 2004; *Melnick*, 2016]. Propagation of slip into deeper, weakly coupled regions of the subduction interface may happen dynamically [e.g., *Kato*, 2007; *Segall and Bradley*, 2012], while deep afterslip may be driven by adjacent, shallow ruptures and represent transfer of elastic energy from shallower portions of the subduction system to beneath the coast [*Helmstetter and Shaw*, 2009; *Briggs*, 2016]. In either case, only a small amount of net uplift—as little as 2 cm per century—is required to satisfy the slow, broad uplift signal recorded geomorphically along the central Andean coastline [*Melnick*, 2016]. At the same time, deep coseismic and postseismic slip generate corresponding regions of subsidence that are incompatible with observations of long-term uplift; thus, it is unclear if these two observations can be reconciled to satisfactorily explain margin-wide vertical displacement patterns over multiple earthquake cycles. Thorough assessment of the role that deep coseismic rupture and afterslip might play in net coastal uplift will require a more complete understanding of the time evolution of afterslip and interseismic strain recovery as well as the vertical displacements generated by viscoelastic processes.

References

- Armijo, R., and R. Thiele (1990), Active faulting in northern Chile: Ramp stacking and lateral decoupling along a subduction plate boundary?, *Earth Planet. Sci. Lett.*, 98(1), 40–61, doi:10.1016/0012-821X(90)90087-E.
- Aron, F., J. Cembrano, F. Astudillo, R. W. Allmendinger, and G. Arancibia (2015), Constructing forearc architecture over megathrust seismic cycles: Geological snapshots from the Maule earthquake region, Chile, *Geol. Soc. Am. Bull.*, 127(3–4), 464–479, doi:10.1130/B31125.1.
- Baba, T., K. Hirata, T. Hori, and H. Sakaguchi (2006), Offshore geodetic data conducive to the estimation of the afterslip distribution following the 2003 Tokachi-oki earthquake, *Earth Planet. Sci. Lett.*, 241(1–2), 281–292, doi:10.1016/j.epsl.2005.10.019.
- Baker, A., R. W. Allmendinger, L. A. Owen, and J. A. Rech (2013), Permanent deformation caused by subduction earthquakes in northern Chile, *Nat. Geosci.*, 6(6), 492–496, doi:10.1038/ngeo1789.

Acknowledgments

The authors thank Associate Editor Emma Hill, Ya-Ju Hsu, Ryan Gold, Nick Beeler, and an anonymous reviewer for their constructive reviews that improved this manuscript. Copernicus Sentinel data 2015 were retrieved from the ASF DAAC in November 2015 and January 2016. GPS time series, including 5 min and daily point position solutions, predicted displacements, and further Sentinel-1a workflows are available upon request from the corresponding author (william-barnhart-1@uiowa.edu). Several figures were generated using the Generic Mapping Tool [Wessel and Smith, 2012]. This work includes a supplement with two tables, four figures, and six data sets. Any use of trade, firm, or product names is for descriptive purposes only and does not imply endorsement by the U.S. Government.

- Barnhart, W. D., and R. B. Lohman (2010), Automated fault model discretization for inversions for coseismic slip distributions, *J. Geophys. Res.*, **115**, B10419, doi:10.1029/2010JB007545.
- Barnhart, W. D., and R. B. Lohman (2013), Phantom earthquakes and triggered aseismic creep: Vertical partitioning of strain during earthquake sequences in Iran, *Geophys. Res. Lett.*, **40**, 819–823, doi:10.1002/grl.50201.
- Beck, S., S. Barrientos, E. Kausel, and M. Reyes (1998), Source characteristics of historic earthquakes along the central Chile subduction Asken et al zone, *J. South Am. Earth Sci.*, **11**(2), 115–129, doi:10.1016/S0895-9811(98)00005-4.
- Bedford, J., et al. (2013), A high-resolution, time-variable afterslip model for the 2010 Maule $M_w = 8.8$, Chile megathrust earthquake, *Earth Planet. Sci. Lett.*, **383**, 26–36, doi:10.1016/j.epsl.2013.09.020.
- Boatwright, J., and M. Cocco (1996), Frictional constraints on crustal faulting, *J. Geophys. Res.*, **101**, 13,895–13,909, doi:10.1029/96JB00405.
- Briggs, R. (2016), Earthquakes: Megathrusts and mountain building, *Nat. Geosci.*, **9**, 346–348, doi:10.1038/ngeo2697.
- Bürgmann, R., S. Ergintav, P. Segall, E. H. Hearn, S. McClusky, R. Reilinger, H. Woith, and J. Zschau (2002), Time-dependent distributed afterslip on and deep below the Izmit earthquake rupture, *Bull. Seismol. Soc. Am.*, **92**(1), 126–137.
- Bürgmann, R., M. G. Kogan, G. M. Steblov, G. Hilley, V. E. Levin, and E. Apel (2005), Interseismic coupling and asperity distribution along the Kamchatka subduction zone, *J. Geophys. Res.*, **110**, B07405, doi:10.1029/2005JB003648.
- Chen, C. W., and H. A. Zebker (2001), Two-dimensional phase unwrapping with use of statistical models for cost functions in nonlinear optimization, *J. Opt. Soc. Am. A*, **18**(2), 338–351.
- Chlieh, M., J. B. D. Chaballier, J. C. Ruegg, R. Armijo, R. Dmowska, J. Campos, and K. L. Feigl (2004), Crustal deformation and fault slip during the seismic cycle in the North Chile subduction zone, from GPS and InSAR observations, *Geophys. J. Int.*, **158**(2), 695–711, doi:10.1111/j.1365-246X.2004.02326.x.
- Chlieh, M., et al. (2007), Coseismic slip and afterslip of the great M_w 9.15 Sumatra–Andaman earthquake of 2004, *Bull. Seismol. Soc. Am.*, **97**(1A), S152–S173, doi:10.1785/0120050631.
- Clift, P. D., and A. J. Hartley (2007), Slow rates of subduction erosion and coastal underplating along the Andean margin of Chile and Peru, *Geology*, **35**(6), 503–506, doi:10.1130/G23584A.1.
- Contreras-Reyes, E., J. Jara, I. Grevenmeyer, S. Ruiz, and D. Carrizo (2012), Abrupt change in the dip of the subducting plate beneath north Chile, *Nat. Geosci.*, **5**(5), 342–345, doi:10.1038/ngeo1447.
- Costantini, M. (1998), A novel phase unwrapping method based on network programming, *IEEE Trans. Geosci. Remote Sens.*, **36**(3), 813–821, doi:10.1109/36.673674.
- Cubas, N., J.-P. Avouac, P. Souloumiac, and Y. Leroy (2013), Megathrust friction determined from mechanical analysis of the forearc in the Maule earthquake area, *Earth Planet. Sci. Lett.*, **381**, 92–103, doi:10.1016/j.epsl.2013.07.037.
- Delouis, B., M. Pardo, D. Legrand, and T. Monfret (2009), The M_w 7.7 Tocopilla earthquake of 14 November 2007 at the southern edge of the northern Chile seismic gap: Rupture in the deep part of the coupled plate interface, *Bull. Seismol. Soc. Am.*, **99**(1), 87–94, doi:10.1785/0120080192.
- DeMets, C., R. G. Gordon, and D. F. Argus (2010), Geologically current plate motions, *Geophys. J. Int.*, **181**(1), 1–80, doi:10.1111/j.1365-246X.2009.04491.x.
- Du, Y., A. Aydin, and P. Segall (1992), Comparison of various inversion techniques as applied to the determination of a geophysical deformation model for the 1983 Borah Peak earthquake, *Bull. Seismol. Soc. Am.*, **82**(4), 1840–1866.
- Ekström, G., M. Nettles, and A. M. Dziewoński (2012), The global CMT project 2004–2010: Centroid-moment tensors for 13,017 earthquakes, *Phys. Earth Planet. Inter.*, **200–201**, 1–9, doi:10.1016/j.pepi.2012.04.002.
- Evans, E. L., and B. J. Meade (2012), Geodetic imaging of coseismic slip and postseismic afterslip: Sparsity promoting methods applied to the great Tohoku earthquake, *Geophys. Res. Lett.*, **39**, L11314, doi:10.1029/2012GL051990.
- Farr, T. G., et al. (2007), The shuttle radar topography mission, *Rev. Geophys.*, **45**(2), doi:10.1029/2005RG000183.
- Grandin, R., E. Klein, M. Métois, and C. Vigny (2016), 3D displacement field of the 2015 M_w 8.3 Illapel earthquake (Chile) from across- and along-track Sentinel-1 TOPS interferometry, *Geophys. Res. Lett.*, **43**, 2552–2561, doi:10.1002/2016GL067954.
- Harris, R. A., and P. Segall (1987), Detection of a locked zone at depth on the Parkfield, California, segment of the San Andreas Fault, *J. Geophys. Res.*, **92**, 7945–7962, doi:10.1029/JB092iB08p07945.
- Hayes, G. P., D. J. Wald, and R. L. Johnson (2012), Slab1.0: A three-dimensional model of global subduction zone geometries, *J. Geophys. Res.*, **117**, B01302, doi:10.1029/2011JB008524.
- Hayes, G. P., M. W. Herman, W. D. Barnhart, K. P. Furlong, S. Riquelme, H. M. Benz, E. Bergman, S. Barrientos, P. S. Earle, and S. Samsonov (2014), Continuing megathrust earthquake potential in Chile after the 2014 Iquique earthquake, *Nature*, **512**, 295–298, doi:10.1038/nature13677.
- Heidarzadeh, M., S. Murotani, K. Satake, T. Ishibe, and A. R. Gusman (2016), Source model of the 16 September 2015 Illapel, Chile, M_w 8.4 earthquake based on teleseismic and tsunami data, *Geophys. Res. Lett.*, **43**, 643–650, doi:10.1002/2015GL067297.
- Helmstetter, A., and B. E. Shaw (2009), Afterslip and aftershocks in the rate-and-state friction law, *J. Geophys. Res.*, **114**, B01308, doi:10.1029/2007JB005077.
- Hsu, Y.-J., M. Simons, J.-P. Avouac, J. Galetzka, K. Sieh, M. Chlieh, D. Natawidjaja, L. Prawirodirdjo, and Y. Bock (2006), Frictional afterslip following the 2005 Nias-Simeulue earthquake, Sumatra, *Science*, **312**(5782), 1921–1926, doi:10.1126/science.1126960.
- Hsu, Y.-J., S.-B. Yu, and H.-Y. Chen (2009), Coseismic and postseismic deformation associated with the 2003 Chengkung, Taiwan, earthquake, *Geophys. J. Int.*, **176**(2), 420–430, doi:10.1111/j.1365-246X.2008.04009.x.
- Igarashi, T., T. Matsuzawa, and A. Hasegawa (2003), Repeating earthquakes and interplate aseismic slip in the northeastern Japan subduction zone, *J. Geophys. Res.*, **108**(B5), 2249, doi:10.1029/2002JB001920.
- Johnson, K. M., J. Fukuda, and P. Segall (2012), Challenging the rate-state asperity model: Afterslip following the 2011 M_9 Tohoku-oki, Japan, earthquake, *Geophys. Res. Lett.*, **39**, L20302, doi:10.1029/2012GL052901.
- Johnson, K. M., A. Mavrommatis, and P. Segall (2016), Small interseismic asperities and widespread aseismic creep on the northern Japan subduction interface, *Geophys. Res. Lett.*, **43**, 135–143, doi:10.1002/2015GL066707.
- Kaneko, Y., J.-P. Avouac, and N. Lapusta (2010), Towards inferring earthquake patterns from geodetic observations of interseismic coupling, *Nat. Geosci.*, **3**(5), 363–369, doi:10.1038/ngeo843.
- Kato, N. (2007), Expansion of aftershock areas caused by propagating post-seismic sliding, *Geophys. J. Int.*, **168**(2), 797–808, doi:10.1111/j.1365-246X.2006.03255.x.
- Kelleher, J. A. (1972), Rupture zones of large South American earthquakes and some predictions, *J. Geophys. Res.*, **77**, 2087–2103, doi:10.1029/JB077i011p02087.
- Kelsey, H., K. Satake, Y. Sawai, B. Sherrod, K. Shimokawa, and M. Shishikura (2006), Recurrence of postseismic coastal uplift, Kuril subduction zone, Japan, *Geophys. Res. Lett.*, **33**, L13315, doi:10.1029/2006GL026052.

- Kelsey, H. M., D. C. Engbreton, C. E. Mitchell, and R. L. Ticknor (1994), Topographic form of the Coast Ranges of the Cascadia Margin in relation to coastal uplift rates and plate subduction, *J. Geophys. Res.*, **99**, 12,245–12,255, doi:10.1029/93JB03236.
- Konca, A. O., et al. (2008), Partial rupture of a locked patch of the Sumatra megathrust during the 2007 earthquake sequence, *Nature*, **456**(7222), 631–635, doi:10.1038/nature07572.
- Langbein, J. (2004), Noise in two-color electronic distance meter measurements revisited, *J. Geophys. Res.*, **109**, B04406, doi:10.1029/2003JB002819.
- Langbein, J. (2012), Estimating rate uncertainty with maximum likelihood: Differences between power-law and flicker–random-walk models, *J. Geod.*, **86**(9), 775–783, doi:10.1007/s00190-012-0556-5.
- Langbein, J., J. R. Murray, and H. A. Snyder (2006), Coseismic and initial postseismic deformation from the 2004 Parkfield, California, earthquake, observed by Global Positioning System, electronic distance meter, creepmeters, and borehole strainmeters, *Bull. Seismol. Soc. Am.*, **96**(4B), S304–S320, doi:10.1785/0120050823.
- Lay, T., and H. Kanamori (1981), An asperity model of large earthquake sequences, in *Earthquake Prediction*, edited by D. W. Simpson and P. G. Richards, pp. 579–592, AGU, Washington, D. C.
- Lin, Y. N., et al. (2013), Coseismic and postseismic slip associated with the 2010 Maule earthquake, Chile: Characterizing the Arauco Peninsula barrier effect, *J. Geophys. Res. Solid Earth*, **118**, 3142–3159, doi:10.1002/jgrb.50207.
- Lloyd, S., S. van der Lee, G. S. França, M. Assumpção, and M. Feng (2010), Moho map of South America from receiver functions and surface waves, *J. Geophys. Res.*, **115**, B11315, doi:10.1029/2009JB006829.
- Lohman, R. B., and W. D. Barnhart (2010), Evaluation of earthquake triggering during the 2005–2008 earthquake sequence on Qeshm Island, Iran, *J. Geophys. Res.*, **115**, B12413, doi:10.1029/2010JB007710.
- Lohman, R. B., and M. Simons (2005), Some thoughts on the use of InSAR data to constrain models of surface deformation: Noise structure and data downsampling, *Geochem. Geophys. Geosyst.*, **6**, Q01007, doi:10.1029/2004GC000841.
- Loveless, J. P., and B. J. Meade (2011), Spatial correlation of interseismic coupling and coseismic rupture extent of the 2011 $M_w = 9.0$ Tohoku-oki earthquake, *Geophys. Res. Lett.*, **38**, L17306, doi:10.1029/2011GL048561.
- Loveless, J. P., R. W. Allmendinger, M. E. Pritchard, J. L. Garraway, and G. González (2009), Surface cracks record long-term seismic segmentation of the Andean margin, *Geology*, **37**(1), 23–26, doi:10.1130/G25170A.1.
- Marone, C. J., C. H. Scholtz, and R. Bilham (1991), On the mechanics of earthquake afterslip, *J. Geophys. Res.*, **96**, 8441–8452, doi:10.1029/91JB00275.
- Meade, B. J. (2007), Algorithms for the calculation of exact displacements, strains, and stresses for triangular dislocation elements in a uniform elastic half space, *Comput. Geosci.*, **33**(8), 1064–1075, doi:10.1016/j.cageo.2006.12.003.
- Melgar, D., W. Fan, S. Riquelme, J. Geng, C. Liang, M. Fuentes, G. Vargas, R. M. Allen, P. M. Shearer, and E. J. Fielding (2016), Slip segmentation and slow rupture to the trench during the 2015, $M_w 8.3$ Illapel, Chile earthquake, *Geophys. Res. Lett.*, **43**, 961–966, doi:10.1002/2015GL067369.
- Melnick, D. (2016), Rise of the central Andean coast by earthquakes straddling the Moho, *Nat. Geosci.*, **9**, 401–407, doi:10.1038/ngeo2683.
- Métis, M., A. Socquet, and C. Vigny (2012), Interseismic coupling, segmentation and mechanical behavior of the central Chile subduction zone, *J. Geophys. Res.*, **117**, B03406, doi:10.1029/2011JB008736.
- Métis, M., C. Vigny, and A. Socquet (2016), Interseismic coupling, megathrust earthquakes and seismic swarms along the Chilean subduction zone (38°–18°S), *Pure Appl. Geophys.*, **173**, 1431–1449, doi:10.1007/s00024-016-1280-5.
- Miyazaki, S., P. Segall, J. Fukuda, and T. Kato (2004), Space time distribution of afterslip following the 2003 Tokachi-oki earthquake: Implications for variations in fault zone frictional properties, *Geophys. Res. Lett.*, **31**, L06623, doi:10.1029/2003GL019410.
- Moreno, M., M. Rosenau, and O. Oncken (2010), 2010 Maule earthquake slip correlates with pre-seismic locking of Andean subduction zone, *Nature*, **467**(7312), 198–202, doi:10.1038/nature09349.
- Motagh, M., B. Schurr, J. Anderssohn, B. Cailleau, T. R. Walter, R. Wang, and J.-P. Villotte (2010), Subduction earthquake deformation associated with 14 November 2007, $M_w 7.8$ Tocopilla earthquake in Chile: Results from InSAR and aftershocks, *Tectonophysics*, **490**(1–2), 60–68, doi:10.1016/j.tecto.2010.04.033.
- Murray, J., and J. Langbein (2006), Slip on the San Andreas Fault at Parkfield, California, over two earthquake cycles, and the implications for seismic hazard, *Bull. Seismol. Soc. Am.*, **96**(4B), S283–S303, doi:10.1785/0120050820.
- Noda, H., and N. Lapusta (2013), Stable creeping fault segments can become destructive as a result of dynamic weakening, *Nature*, **493**(7433), 518–521, doi:10.1038/nature11703.
- Nur, A., and G. Mavko (1974), Postseismic viscoelastic rebound, *Science*, **183**(4121), 204–206, doi:10.1126/science.183.4121.204.
- Ortlieb, L., S. Barrientos, and N. Guzman (1996), Coseismic coastal uplift and coralline algae record in northern Chile: The 1995 Antofagasta earthquake case, *Quat. Sci. Rev.*, **15**(8), 949–960, doi:10.1016/S0277-3791(96)00056-X.
- Perfettini, H., and J.-P. Avouac (2007), Modeling afterslip and aftershocks following the 1992 Landers earthquake, *J. Geophys. Res.*, **112**, B07409, doi:10.1029/2006JB004399.
- Plafker, G., and J. C. Savage (1970), Mechanism of the Chilean earthquakes of May 21 and 22, 1960, *Geol. Soc. Am. Bull.*, **81**(4), 1001–1030, doi:10.1130/0016-7606(1970)81[1001:MOTCEO]2.0.CO;2.
- Pollitz, F. F., R. Bürgmann, and P. Banerjee (2006), Post-seismic relaxation following the great 2004 Sumatra-Andaman earthquake on a compressible self-gravitating Earth, *Geophys. J. Int.*, **167**(1), 397–420, doi:10.1111/j.1365-246X.2006.03018.x.
- Pritchard, M. E., and M. Simons (2006), An aseismic slip pulse in northern Chile and along-strike variations in seismogenic behavior, *J. Geophys. Res.*, **111**, B08405, doi:10.1029/2006JB004258.
- Pritchard, M. E., M. Simons, P. A. Rosen, S. Hensley, and F. H. Webb (2002), Co-seismic slip from the 1995 July 30 $M_w = 8.1$ Antofagasta, Chile, earthquake as constrained by InSAR and GPS observations, *Geophys. J. Int.*, **150**(2), 362–376, doi:10.1046/j.1365-246X.2002.01661.x.
- Rice, J. R. (1993), Spatio-temporal complexity of slip on a fault, *J. Geophys. Res.*, **98**, 9885–9907.
- Ruiz, S., et al. (2013), The Constitución earthquake of 25 March 2012: A large aftershock of the Maule earthquake near the bottom of the seismogenic zone, *Earth Planet. Sci. Lett.*, **377**–378, 347–357, doi:10.1016/j.epsl.2013.07.017.
- Sambridge, M. (1999), Geophysical inversion with a neighbourhood algorithm—I. Searching a parameter space, *Geophys. J. Int.*, **138**(2), 479–494, doi:10.1046/j.1365-246X.1999.00876.x.
- Savage, J. C. (1983), A dislocation model of strain accumulation and release at a subduction zone, *J. Geophys. Res.*, **88**, 4984–4996, doi:10.1029/JB088iB06p04984.
- Sawai, Y., K. Satake, T. Kamataki, H. Nasu, M. Shishikura, B. F. Atwater, B. P. Horton, H. M. Kelsey, T. Nagumo, and M. Yamaguchi (2004), Transient uplift after a 17th-century earthquake along the Kuril subduction zone, *Science*, **306**(5703), 1918–1920, doi:10.1126/science.1104895.
- Scholz, C. H. (1998), Earthquakes and friction laws, *Nature*, **391**(6662), 37–42, doi:10.1038/34097.

- Segall, P., and A. M. Bradley (2012), Slow-slip evolves into megathrust earthquakes in 2D numerical simulations, *Geophys. Res. Lett.*, **39**, L18308, doi:10.1029/2012GL052811.
- Sparkes, R., F. Tilmann, N. Hovius, and J. Hillier (2010), Subducted seafloor relief stops rupture in South American great earthquakes: Implications for rupture behaviour in the 2010 Maule, Chile earthquake, *Earth Planet. Sci. Lett.*, **298**(1–2), 89–94, doi:10.1016/j.epsl.2010.07.029.
- Storchak, D. A., D. D. Giacomo, I. Bondár, E. R. Engdahl, J. Harris, W. H. K. Lee, A. Villaseñor, and P. Bormann (2013), Public release of the ISC–GEM Global Instrumental Earthquake Catalogue (1900–2009), *Seismol. Res. Lett.*, **84**(5), 810–815, doi:10.1785/0220130034.
- Suito, H., and J. T. Freymueller (2009), A viscoelastic and afterslip postseismic deformation model for the 1964 Alaska earthquake, *J. Geophys. Res.*, **114**, B11404, doi:10.1029/2008JB005954.
- Tilmann, F., et al. (2016), The 2015 Illapel earthquake, central Chile: A type case for a characteristic earthquake?, *Geophys. Res. Lett.*, **43**, 574–583, doi:10.1002/2015GL066963.
- Tong, X., et al. (2010), The 2010 Maule, Chile earthquake: Downdip rupture limit revealed by space geodesy, *Geophys. Res. Lett.*, **37**, L24311, doi:10.1029/2010GL045805.
- Tse, S. T., and J. R. Rice (1986), Crustal earthquake instability in relation to the depth variation of frictional slip properties, *J. Geophys. Res.*, **91**, 452–459, doi:10.1029/JB091iB09p09452.
- Wang, K., Y. Hu, and J. He (2012), Deformation cycles of subduction earthquakes in a viscoelastic Earth, *Nature*, **484**(7394), 327–332.
- Wessel, P., and W. H. F. Smith (1998), New, improved version of generic mapping tools released, *Eos Trans. AGU*, **79**(47), 579, doi:10.1029/98EO00426.
- Yabuki, T., and M. Matsu'ura (1992), Geodetic data inversion using a Bayesian information criterion for spatial distribution of fault slip, *Geophys. J. Int.*, **109**(2), 363–375, doi:10.1111/j.1365-246X.1992.tb00102.x.
- Yagi, Y., M. Kikuchi, and T. Nishimura (2003), Co-seismic slip, post-seismic slip, and largest aftershock associated with the 1994 Sanriku-haruka-oki, Japan, earthquake, *Geophys. Res. Lett.*, **30**(22), 2177, doi:10.1029/2003GL018189.